Journal of Structural Geology 33 (2011) 819–832

Contents lists available at ScienceDirect

Journal of Structural Geology

journal homepage: www.elsevier.com/locate/jsg

Fabric development in a weathering profile at a basement–cover interface, the sub-Cambrian peneplain, Israel: Implications for decollement tectonics

T. Angerer [a,*,1], R.O. Greiling [a], D. Avigad [b]

[a] Institut für Angewandte Geowissenschaften, Strukturgeologie & Tektonophysik, Karlsruhe Institute of Technology, Hertzstrasse 16, 76187 Karlsruhe, Federal Republic of Germany
[b] Institute of Earth Sciences, Hebrew University, Givat Ram, Jerusalem 91904, Israel

ARTICLE INFO

Article history:
Received 26 March 2010
Received in revised form
11 March 2011
Accepted 11 March 2011
Available online 21 March 2011

Keywords:
Anisotropy of magnetic susceptibility
Basement-cover interface
Decollement
Palaeoweathering
Roded granite

ABSTRACT

The present study examines a fossil saprock–saprolite–laterite-profile beneath the sub-Cambrian peneplain in the Pan-African Roded Granite, Israel, with regard to structure and magnetic fabrics (anisotropy of magnetic susceptibility, AMS), and image analysis of compaction. The deformed granite shows two pre-weathering foliations, S_{1m} (magmatic) and S_{2g} (gneissic). Pre-Early Cambrian weathering comprised weathering-brecciation in saprock and saprolite, and chemical weathering with clay-formation in saprolite and laterite. During subsequent Phanerozoic burial the laterite was vertically compacted to 73% of its original thickness. In the laterite, compaction produced an unconformity-parallel cleavage (S_{3d}) with increasing intensity towards the unconformity. Bulk susceptibility (κ_{bulk}) and anisotropy (P') decrease from the unweathered granite into the saprolite, as a result of progressive magnetite breakdown, martitization and weathering-brecciation. In the laterite, an enrichment of haematite and relic Fe–Mg–mica lead to increased κ_{bulk}. Here, magnetic fabrics trace the compaction fabrics. The sub-horizontal, compactional clay–/mica-fabric S_{3d} defines a structurally weak and impermeable layer. The mechanical weakness of a clay-enriched weathering horizon with an unconformity-parallel, planar shape-preferred orientation, combined with the potentially overpressured state due to the sealing character of such a zone provides a viable explanation for the abundant localization of decollement horizons at or beneath basement-cover interfaces.

1. Introduction

Shear zones close to basement–cover interfaces play a key role in the structural evolution of the earth's crust as major decollement surfaces in both extensional and contractional regimes. For example, such decollements may occur in extensional metamorphic core complexes (Lister and Davis, 1989; Roberts and Yielding, 1994) or at the base of accretionary or orogenic wedges (Coward, 1994; Nemcok et al., 2005). Geometry and mechanics of such wedges are dependent on their internal strength and the strength of their base. Accordingly, orogenic wedges develop basal shear zones at horizons with a low strength, for instances evaporites (Himalayas, Zagros, Jura belt of the Alps: Madritsch et al., 2008; Streule et al., 2010) or shales (Gee et al., 2008). In these examples, the basal decollement is situated close to, but above the basement–cover interface. However, orogenic wedges frequently incorporate slices of basement rocks (e.g., Caledonides of NW Scotland: Butler et al., 2006; Law et al., 2010; Streule et al., 2010), where the basal decollement horizon is situated beneath the basement–cover interface. There, it is not a priori clear, why the basement rocks are mechanically weak. A plausible explanation may be fossil palaeoweathering zones with fabrics and geometries related to palaeoweathering and diagenesis, which are developed and preserved beneath basement–cover interfaces. The development of abundant clay minerals may assist the occurrence of preferred mineral orientations (SPO, LPO) that can influence permeability, fluid pressure and frictional strength of the basement prior to cover sedimentation (e.g., Wintsch et al., 1995 and references therein). However, studies about properties and deformation of fossil palaeoweathering profiles are rare (e.g., Migon and Lidmar, 2001; Nesbitt and Young, 1989; Retallack, 1991), and only a few magnetic fabric (anisotropy of magnetic susceptibility, AMS) studies characterized (recent) relic weathering profiles (Mathe et al., 1997).

Therefore, the present study addresses two questions: what are the structural and mineralogical properties of weathered interfaces? Can the strain and fabric change in the altered rock be

* Corresponding author. Tel.: +61 8 64887150.
E-mail address: t.angerer@web.de (T. Angerer).
[1] Present address: Centre for Exploration Targeting, Department of Earth and Environmental Science, University of Western Australia, M006, 35 Stirling Highway, Crawley, WA 6009, Australia.

0191-8141/$ – see front matter © 2011 Elsevier Ltd. All rights reserved.
doi:10.1016/j.jsg.2011.03.010

quantified? With a focus on the rock and magnetic fabrics (AMS) of a fossil lateritic palaeoweathering profile, this study documents the general fabric evolution and porosity, and changes of magnetic minerals and associated magnetic fabrics (AMS) during early tectonics, hydrothermal alteration, paedogenesis and subsequent diagenesis. The investigated profile is preserved on a continental shield, the Arabian-Nubian Shield, since c. 550 Ma ago, and was not subjected to subsequent orogenic deformation.

2. Regional geology

The Roded Block in southern Israel is one of the northernmost basement outcrops of the Arabian-Nubian Shield (ANS, Fig. 1). There, the Roded Granite belongs to a series of late- to post-orogenic Pan-African granitoids that intruded the ANS in the late Neoproterozoic (e.g., Bentor, 1985). ANS quartz-diorite has an intrusion age of 634 ± 2 Ma (U/Pb on zircons: Katz et al., 1998) and was locally ductilely deformed during latest Pan-African orogeny. Erosion took place since 550 Ma ago (Garfunkel, 2002; Jarrar et al., 1993). Its northern part was subsequently covered by continental redbeds and then by shallow marine sandstones in the Middle Cambrian (Garfunkel, 2002; Weissbrod, 1980). The top of the eroded basement just beneath the Cambrian sandstone contains a spectacular saprolitic weathering horizon locally reaching tens of metres in thickness at this interface. The horizon formed as a consequence of extensive chemical weathering that affected widespread continental areas at the end of Pan-African orogeny and produced the great lower Palaeozoic quartz-rich sandstones (Avigad et al., 2005).

The Roded Granite shows a complex geological history: 1) synkinematic emplacement of the Roded Granite in late Pan-African times; 2) weathering and peneplanation after the Pan-African orogeny (Garfunkel, 1999, 2002; Stern, 2002), at about 530 ± 10 Ma (Jarrar et al., 1993), yielding a saprock–saprolite–laterite weathering profile (Angerer, 2007); 3) Phanerozoic burial stage when the laterite was vertically compacted; and 4) Tertiary involvement in the tectonics of the Dead Sea Transform (Ben-Avraham and Lazar, 2006; Garfunkel, 1993; Sobolev et al., 2005), which caused local cataclastic deformation within the Roded Block.

We sampled the weathering profile of the Roded Granite beneath the unconformable base of the Cambrian redbeds: from "fresh" granite through moderately weathered granite (saprock), intensely weathered granite (saprolite) to ferricrete, here named laterite (Figs. 2 and 3).

3. Petrography in the weathering zones

3.1. Fresh granite

The Roded Granite is a calc-alkaline granite (Druckman et al., 1993). Samples RA3-1 and RA1-5a (which is a corestone within saprock) provide the compositional and textural data for fresh granites (Fig. 2). The grey to red-coloured granite has a sub-equigranular texture with crystal sizes of 2–10 mm. Major components are plagioclase, quartz and K-feldspar, and minor components are biotite, chlorite and white mica, which are commonly present as chlorite-mica stacks (approximately 20 vol%; chlorite-dominated, with intercalated biotite and white mica). Subhedral to anhedral

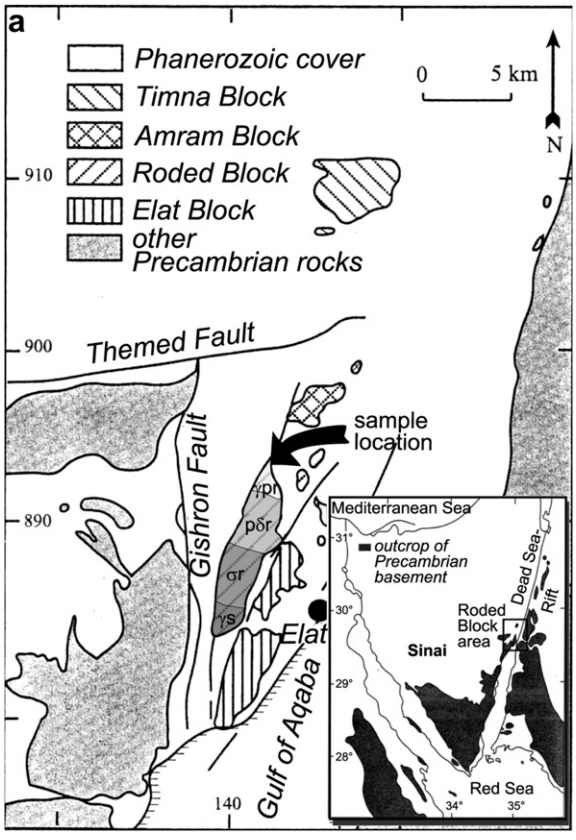

Fig. 1. Geological map of the Roded Block region (arrow points to study area). The Roded Block is divided from North to South into Roded Granite (γpr), Roded Quartz Diorite (pδr), Roded Schist, Gneiss, Migmatite (σr), and Shahmon Granite (γs). The inset shows the locality of the Roded Block region (square) at the northern margin of the exposed Arabian-Nubian Shield (black), modified after Garfunkel (1980) and Gutkin and Eyal (1998).

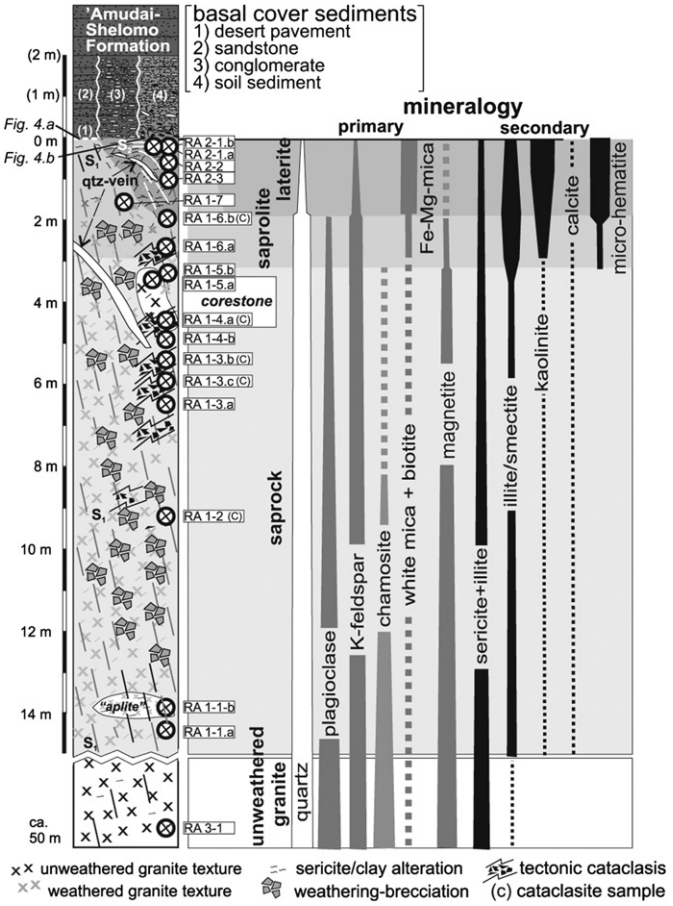

Fig. 2. The Roded Granite weathering profile, with sample locations and primary and secondary (i.e, alteration, weathering) mineralogy.

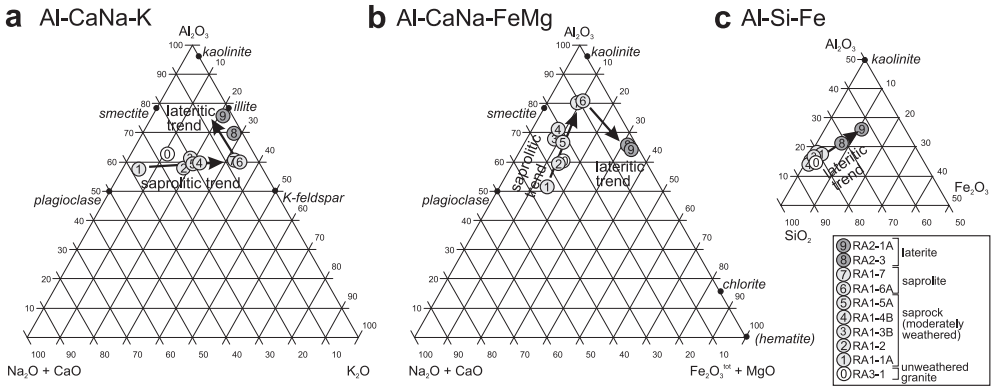

Fig. 3. Whole rock geochemical data showing saprolitic and lateritic weathering trends: (a) the Al–CaNa–K ternary diagram shows substantial Na_2O (and minor CaO) depletion and relatively stable K_2O contents; (b) the Al–CaNa–FeMg diagram shows $Fe_2O_{3(total)}$ + MgO enrichment relative to Al_2O_3; (c) the Si–Al–Fe diagram indicates only a lateritic trend, characterized by SiO_2 depletion. For comparison, mineral compositions are plotted (modified after Angerer, 2007).

(titaniferous) martite (haematite pseudomorphous after magnetite), rutile, titanite, calcite, epidote, apatite and zircon are present. Feldspar is strongly sericitized and chlorite partially altered, brownish coloured and impregnated with red microcrystalline haematite crystals, rutile and titanite.

Two texture/fabric types are distinguishable: "macroscopically undeformed granite" (Fig. 4c) and "foliated granite" (Fig. 4d). The macroscopically undeformed granite has a weak preferred orientation of the chlorite-mica stacks (Angerer, 2007). Quartz and feldspar are rarely elongated but show undulatory extinction. Subhedral titaniferous martite grains are often elongated. This fabric is an incipient schistosity and named S_{1m}. It dips steeply and trends in E–W direction.

In the foliated granite, a gneissic schistosity (S_{2g}) is well defined by the chlorite-mica stacks, which are more abundant than in the macroscopically undeformed granite. Quartz grains are mostly elongate parallel with the foliation and are frequently dynamically recrystallized. Evidence such as subgrain rotation and grain boundary migration for recrystallization are observed. The undulatory extinction of feldspar crystals is similar to that in macroscopically undeformed granite. The S_{2g} has two conjugate sets that both trend northeast with different dip directions (Fig. 5a). Locally, an N–S trend of S_{2g} is observed.

Ductile deformation occurred prior to weathering/erosion because microstructures in the laterite show relics of S_{2g} surfaces. The S_{2g} schistosity can be related to the late Pan-African compressional to transpressional deformation of in the Roded block (Katz et al., 1998) in terms of P/T conditions, kinematics (steep E–NE striking, structures compatible to compression/transpression with E–W directed principal stress), and timing between intrusion during late Pan-African time and Neoproterozoic-Cambrian erosion. Ductile deformation during the Phanerozoic is not recorded in the ANS for this region (Katz et al., 1998).

3.2. Saprock (moderately weathered granite)

The dominant weathered zone in the profile is a saprock zone. The saprock, defined as a moderately weathered rock (c.f., Anand and Paine, 2002), is characterized by textures similar to the unweathered granite, and brownish to reddish colours due to haematite-clay-rich chemical weathering (Fig. 4e). Further alteration minerals are sericite–illite, which are located mostly along joints. Chlorite-mica stacks are partly altered to kaolinite and haematite–titanite–TiO_2-mixture.

The textural cohesion of large parts of the saprocks is slightly reduced by rock fragmentation with cm-scale spacing ("weathering-brecciation"). Along the joints, primary minerals have a reduced grain size and secondary clay is present, whereas between joints, the granite is unaffected, including preservation of S_{2g}.

3.3. Saprolite/pallid zone (intensely weathered granite)

The saprolite zone is characterized by strongly altered granite with an almost white colour (Fig. 4f). This pallid zone is typically found in a lateritic weathering profile just underneath indurated (sub-)soil material (Stephens, 1946; Tardy, 1992). Plagioclase and chlorite are more kaolinitized in the saprolite than in the saprock. Kaolinite, quartz, and microcline are the main saprolite constituents. Chlorite-mica stacks yield mica-kaolinite-stacks, enriched in secondary Fe-oxides (mainly haematite) and TiO_2, presumably anatase. This mica is referred to as Fe–Mg–mica. Abundant haematite and titaniferous minerals in the Fe–Mg–micas result from the (1) chlorite inclusions of the unweathered granite, and (2) kaolinization of chlorite.

The primary granitic texture is generally intact, however, much of the rock is friable due to intense "weathering-brecciation" and alteration of feldspar. S_{2g}, where developed, is preserved in the saprolite.

3.4. Laterite

The transitional zone from the saprolitic pallid zone to the lateritic ferricrete is typically several decimetres thick, and appears mottled (c.f., Stephens, 1946; Tardy, 1992), due to red clay-mica concretions in a pale saprolite matrix with granitic texture. Concretion abundance increases upwards until white rock fractions disappear. A weakly indurated, clayey horizon is the uppermost part of the preserved palaeoweathering profile, the laterite. It occupies the uppermost 2 m beneath the unconformity. This lateritic ferricrete lithology is dominated by Fe–Mg–micas and clay minerals (30 vol%), and depleted in quartz and K-feldspar (together 10 vol%) (Fig. 4g). Dissolution of primary feldspars led to a macro-porosity (c.f., Boivin et al., 2005), which can be observed throughout the laterite texture (Fig. 4h). The matrix is mainly haematite-impregnated kaolinite, which causes a purple–red colour. Quartz occurs as primary crystals, as well as small mm–cm size exsolution rods. These quartz rods are exclusively observed in the laterite. K-feldspars are mostly kaolinized, but relic cores occur in the matrix.

At the base of the laterite, a strong shape preferred orientation (SPO) of Fe–Mg mica stacks produces a steep cleavage, which is clearly a continuation of S_{2g} in the foliated rocks below. With proximity to the unconformity, this foliation rotates toward shallow dips. As a consequence, an unconformity-parallel, i.e., almost horizontal, foliation, S_{3d}, defined by Fe–Mg–mica SPO and

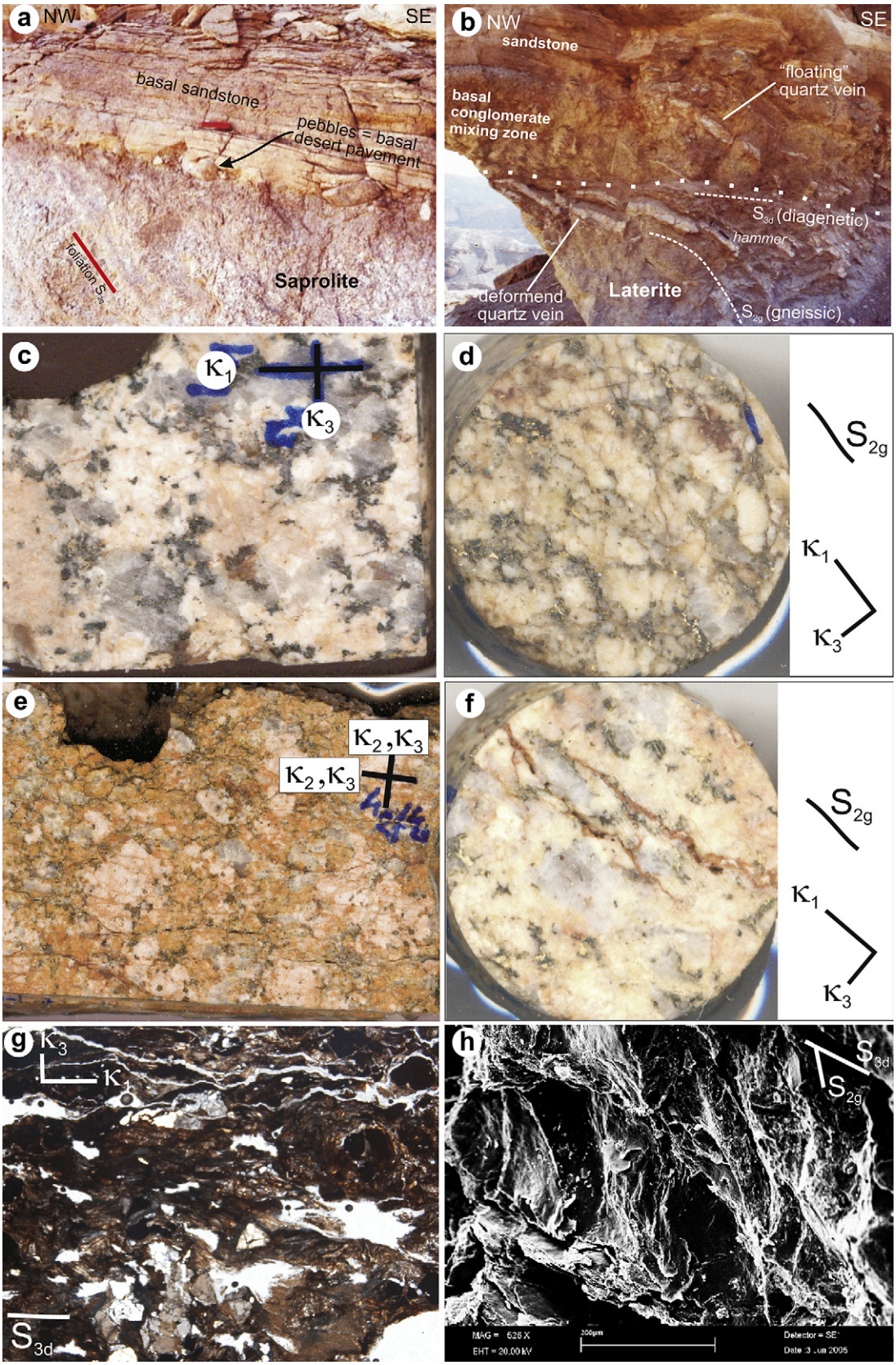

Fig. 4. (a) Outcrop photograph showing the saprolite with relic gneissic foliation, unconformably overlain by a sandstone of the Amudai Shelomo Formation. A basal layer of pebbles is a desert pavement and marks the unconformity; (b) outcrop photograph showing the laterite and the sedimentary cover. The laterite shows relics of primary granite foliation and an unconformity-parallel texture. A quartz vein is rotated and faulted; (c) hand specimen of macroscopically undeformed granite (RA3-1, long side 8 cm); (d) AMS-cylinder of the foliated granite (RA1-1a, 25 mm diameter); (e) hand specimen of the weathering-breccia with relatively fresh microcline (red) in weathered plagioclase (brown) matrix (RA1-5b, long side 10 cm); (f) AMS-cylinder of a saprolite, which shows a weak foliation (RA1-7, 25 mm diameter); (g) micrograph of laterite texture with a preferred orientation of micas (RA2-1b, long side 4.85 mm); (h) SEM image of a laterite zone with preserved crenulation cleavage, S_{3d} (shallow dip towards right) overprinting steep S_{2g} (RA2-1b). (For interpretation of the references to colour in this figure legend, the reader is referred to the web version of this article.)

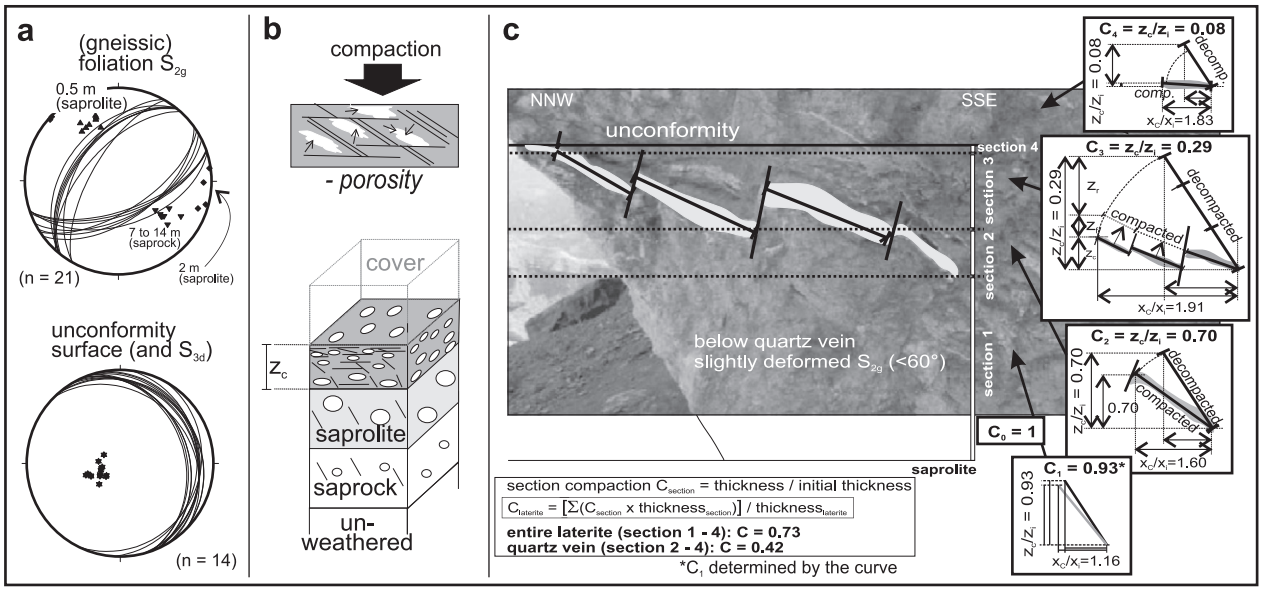

Fig. 5. Structural analysis of the weathering profile: (a) stereographic projection of the unconformity surface and foliations in granite; (b) schematic compaction and volume calculation with porosity decrease in the laterite; (c) image analysis of an outcrop photograph: determination of the vertical compaction of four sections in the laterite using a deformed and tilted quartz vein as a marker.

quartz-rods, is developed in the uppermost metre (Figs. 4g and 5a). The S_{3d} cuts across S_{2g} (Fig. 4h), and thus the S_{2g}-deflection is a result of the progressive overprint of S_{3d}. Locally, S_{3d} reaches down to the lower saprolite boundary as an effect of disintegration due to very strong weathering-brecciation. Larger quartz veins in the laterite are inherited from the granite and show rotation and brecciation (Fig. 4b).

4. Methods of magnetic analyses

In addition to optical observations, the magnetic minerals are identified by temperature dependent susceptibility measurements $\kappa(T)$. This method is well documented (Kontny and de Wall, 2000; Kontny et al., 2004; Tauxe, 2002). For the $\kappa(T)$ analyses c. 0.25 cm^3 of crushed sample material from each sample is measured. The grain size spectrum is up to 0.5 mm. The measurements were conducted using the KLY-2 Kappa bridge (300 A/m at 920 Hz) combined with CS-2 (for high temperature) and CS-L (for low temperature; all from AGICO, Brno, Czech Republic) units in a temperature range of −192 to 700 °C. Measurements are done in an Argon atmosphere to minimize oxidation during heating. For further description see Hrouda (1994).

The low-field anisotropy of magnetic susceptibility (AMS) of the samples was measured with a KLY-2 Kappa bridge at the Geological–Palaeontological Institute of the University of Heidelberg on 1 inch standard cylinders (three–six per sample). The resulting data for each specimen are the bulk susceptibility tensor (volume susceptibility κ_{bulk} in SI units) and three principal axes ($\kappa_1 \geq \kappa_2 \geq \kappa_3$) of an AMS-ellipsoid with their geographically corrected orientations (Daly and Henry, 1983). The corrected anisotropy degree P′ (eccentricity) and shape factor T (ellipsoid shape) are calculated from κ_{bulk} and the principal axes (Jelinek, 1981; Tarling and Hrouda, 1993).

5. Petrophysical characteristics of the weathering zones

5.1. Bulk density and porosity

The bulk density ρ of the unweathered granite is 2460 kg/m^3. It decreases in the saprolite to 2320 kg/m^3 ρ does not change across the saprolite–laterite boundary (saprolite: 2320 kg/m^3, lower laterite 2310 kg/m^3), whereas it increases slightly within the laterite to 2380 kg/m^3.

The porosity ϕ is a critical parameter with respect to compaction, bulk density and permeability characteristics of the laterite. The present laterite has a well developed macro-porosity (c.f., Boivin et al., 2005), which is the void space created by weathering-related dissolution of large primary feldspar and quartz (Fig. 5b). These larger void spaces are typically bounded by a "framework-like" crenulation fabric of micaceous S_{2g} surfaces and S_{3d}-surfaces (Fig. 4h). Porosities of representative samples were calculated using measured values of bulk and grain density. The fresh granite RA3-1 shows a very small porosity with $\phi = 0.04$, the saprolite sample RA1-7 a moderately large porosity with $\phi = 0.27$ (Fig. 4b, c). The largest porosity is measured in the lower laterite sample ($\phi = 0.34$), whereas a decrease is observed in the upper laterite sample ($\phi = 0.24$).

5.2. Vertical compaction in the laterite

Petrographic observations and geochemical mass balance calculations (Angerer, 2007) demonstrate that rocks in the saprolite are not compacted, whereas the laterite shows increasing compaction towards the unconformity (see section 3.4, and AMS studies below). A quartz vein crosscutting the Roded Granite provides an additional marker for the compaction.

We used geometrical restoration by image analysis of the quartz vein to its pre-compaction state to determine the compaction magnitude.

The laterite horizon is divided into four sections with different degrees of vein rotation, and hence compaction magnitudes (Table 1). Compaction for each section, referred to as C_1 (bottom) to C_4 (top; Fig. 5), respectively, is the measured thickness z_w divided by the initial thickness z_i (Caudill et al., 1997). The initial thickness is the sum of z_w and the rotational and fault increments, z_r and z_f, respectively.

$$C_{section} = z_c/z_i = z_c/\left(z_c + z_r + z_f\right) \quad (1)$$

The bulk compaction of the laterite is the weighted mean of the section compaction, i.e. the sum of the products $C_{section} \times z_{c(section)}$,

Table 1
Compilation of data shown as graphs in Fig. 6 (n.d. = not determined, *= estimated by petrography, **= by curve fitting, see Angerer, 2007).

	Distance from unconformity [m]	Compaction $C = z_c/z_i$	Porosity ϕ	Bulk density ρ [kg/m^3]	κ_{bulk} [10^{-6}] SI	κ_3 incl. [°]	P′
Entire laterite (average)	0–2	0.73	0.29	2340	–	–	–
Section 4	0–0.05	0.08	n.d.	n.d.	–	–	–
Section 3	0.05–0.55	0.29	n.d.	n.d.	–	–	–
at RA2-1b	0.2	0.22	0.24	2380	432	82	1.010
at RA2-2	0.5	n.d.	n.d.	n.d.	433	60	1.030
Section 2	0.55–0.84	0.70	n.d.	n.d.	–	–	–
Section 1	0.84–2	0.93**	n.d.	n.d.	–	–	–
at RA2-3	1	0.85	0.34	2310	417	26	1.016
Saprolite, foliated (RA1-7)	1	1*	0.27	2320	76	16	1.039
Saprock, foliated (RA1-1A)	14.5	1*	n.d.	n.d.	486	32	1.085
Unweathered granite (RA3-1)	>15	1*	0.04	2460	1513	33.7	1.064

divided by the thickness of the entire laterite, which is the sum of z_w of each section:

$$C_{laterite} = \left[\sum\left(C_{section} \times z_{c(section)}\right)\right] \Big/ \sum z_{w(section)} \quad (2)$$

The quartz vein fraction in section 4, just beneath the unconformity, is almost parallel to the unconformity. Here, compaction is at a maximum ($C_4 = 0.08$; Fig. 5c). In section 3, finite compaction is a result of rotation and a fault increment ($C_3 = 0.29$), and in section 2 it is much less ($C_2 = 0.70$). In the lowermost section 1, the quartz vein is not observed, but the steep dip of the cleavage S_{2g} indicates a very small compaction. C_1 of 0.93 was determined by curve extrapolation. The change in compaction with position in the laterite horizon follows a logarithmic compaction curve (Fig. 6a). Bulk compaction $C_{laterite}$ is 0.73 (Eq. (2)).

Pre-compaction porosity (ϕ_w), mostly macro-porosity in the laterite is a function of weathering degree (Angerer, 2007: see chemical alteration and plagioclase alteration indices), and increases upward in the laterite profile. However, petrography shows that the macro-porosity is reduced in the upper laterite due to vertical compaction in this zone. This explains why the measured (post-compaction) porosity (ϕ) decreases in the upper laterite (Fig. 6a, b, Table 1). The porosity in the buried laterite is therefore the result of the complex interplay between chemical weathering (that led to an increase of porosity) and later compaction (that decreased porosity).

The unchanged bulk density (ρ) within the saprolite–laterite transition zone is a trade-off between increased porosity and increased residual heavy minerals from soil formation (Table 1). The increase of ρ from the lower to the upper laterite is attributed to the strong burial compaction. Bulk density is therefore, like porosity, dependent on both weathering and compaction.

6. Magnetomineralogy in the weathering zones (κ_{bulk} and κ (T)-curves)

Bulk susceptibilities (κ_{bulk}) are quite variable in the granite reaching from 600 to 2800 $\times$ 10^{-6} [SI] (Fig. 7a, Table 2). The saprock shows medium κ_{bulk} values between 200 and 1095 $\times$ 10^{-6} [SI] and the saprolite has smallest values between 50 and 105 $\times$ 10^{-6} [SI]. The κ_{bulk} of >600 $\times$ 10^{-6} [SI] in the corestone granite implies that martite contains a significant amount of magnetite remnants. The laterite displays medium values between 300 and 1000 $\times$ 10^{-6} [SI] (Fig. 7a, Table 2).

In the granite, magnetite is indicated by the characteristic Curie temperature (T_{Curie}) in the range between 570 and 590 °C, and the Verwey transition (T_{Verwey}) at ca. −150 °C (Fig. 8a) points to multidomain magnetite (Just et al., 2004; Kontny and de Wall, 2000). The κ(T)-curves of the granite are not reversible, and the susceptibility is by a factor 4.24 [$\kappa_{cool}/\kappa_{heat}$ index, which is calculated as $\kappa(T_{after\ heating})/\kappa(T_{before\ heating})$] greater after the heating experiment. This susceptibility increase is related to magnetite formation and can be interpreted as a reduction of existing martite to magnetite during the experiment (Just, 2005).

The κ(T)-curve of the saprock is very similar to the one for the granite (Fig. 8b). The $\kappa_{cool}/\kappa_{heat}$ index of 5.37 is slightly greater than for the protolith. A hump in the cooling curve in the temperature range of 250 °C–400 °C may be related to maghemitization.

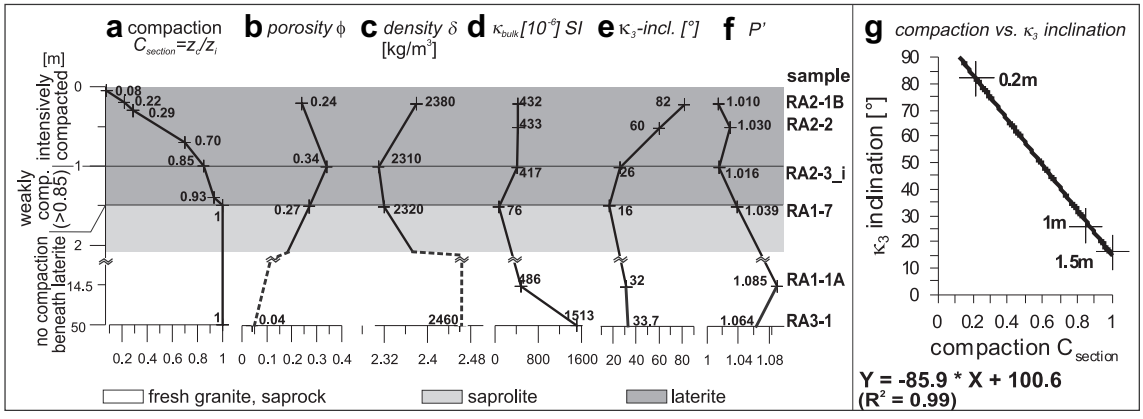

Fig. 6. Compilation of laterite data. (a) vertical compaction (see Fig. 5); (b) porosity; (c) bulk rock density; (d) bulk magnetic susceptibility; (e) inclination of pole to magnetic foliation; (f) corrected magnetic anisotropy degree; (g) binary plot showing the linear relationship between compaction and κ_3 inclination in laterite.

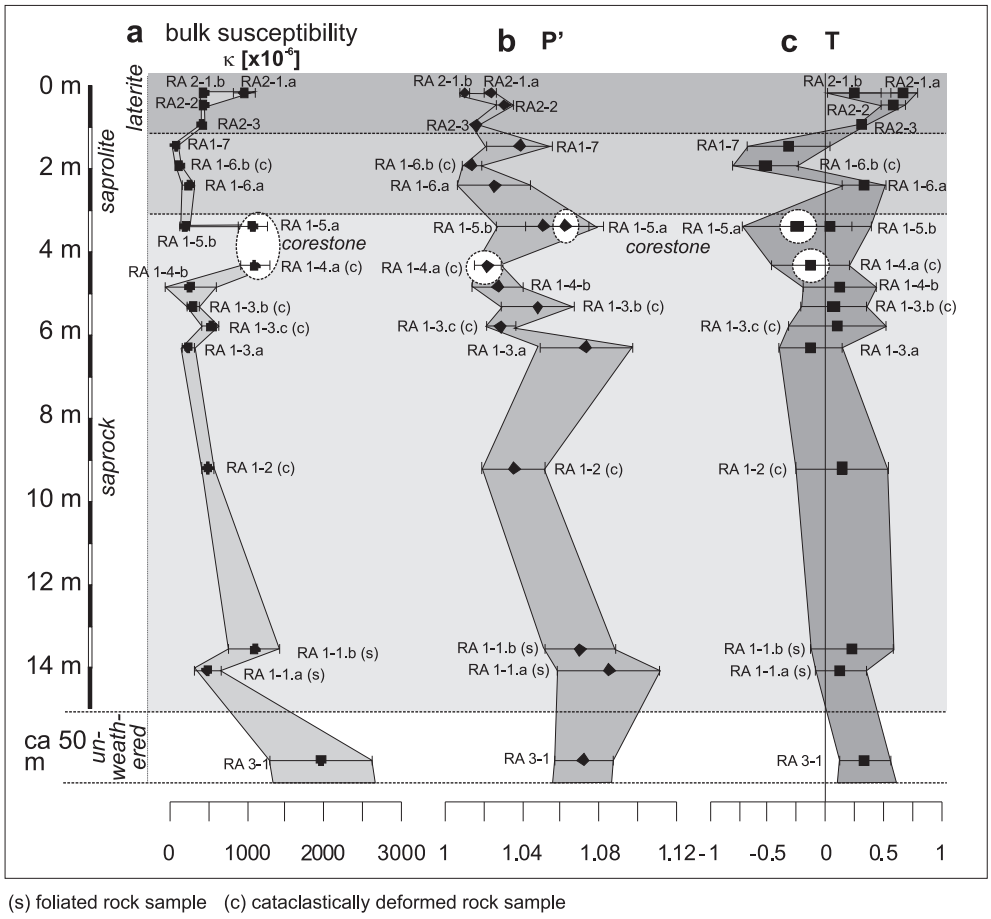

Fig. 7. Magnetic susceptibility properties of samples in the weathering profile: (a) bulk magnetic susceptibility κ_{bulk}; (b) corrected anisotropy degree P′; (c) shape factor T.

The κ(T)-curve of the saprolite sample shows also a magnetite T_{Curie} (Fig. 8c), but during further heating a continuous decrease in susceptibility is observed from 640 up to 700 °C. This behaviour points to microcrystalline haematite, although a κ decrease at T_{Curie} of haematite is not indicated. The slightly lower $\kappa_{cool}/\kappa_{heat}$ index of 3.13, compared to saprock and fresh granite, is associated with phyllosilicates and microcrystalline haematite contributing to κ_{bulk}.

The κ(T)-curve of the laterite indicates a predominance of paramagnetic minerals (Fe–Mg–micas, iron-bearing illite) evidenced by the 1/κ decrease with increasing temperature in the low-temperature range (Fig. 8d). During heating, susceptibility drops down to paramagnetic values at a temperature of about 580 °C, thus indicating the presence of magnetite. During further heating a sudden drop at 670 °C indicates a T_{Curie} typical for haematite. The cooling curve is almost reversible ($\kappa_{cool}/\kappa_{heat}$ index 1.09). It appears that microcrystalline haematite does not reduce to magnetite during the experiment like martite does, an observation also documented by Just (2005).

7. AMS fabric types in the weathering zones

The anisotropy degree P′ varies in unweathered and macroscopically undeformed granite between 1.04 and 1.09 with a standard deviation of ±0.01 or 0.02 (Fig. 9). Shapes are mainly oblate ($T > 0.34 \pm 0.22$). In the saprocks, T scatters from oblate to prolate. In the saprolite, P′ is small ($<1.033 \pm 0.02$) and T scatters between −0.5 and 0.5. Laterite samples have small P′ values ($<1.04 \pm 0.005$), and exclusively oblate shapes. Samples with a S_{2g} foliation have the largest eccentricities in the profile, $P' = 0.11$. Here, shapes are slightly oblate ($0 < T < 0.5$, two specimens with $T < 0$). Rocks that experienced cataclasis through the weathering stages, generally show a low P′ ranging between 1 and 1.07 ± 0.02, and T is scattered throughout oblate and prolate fields ($-0.4 < T < 0.4$).

The generally high variability of P′ and T (Fig. 7) within the weathering profile is explainable as a result of the superposition of primary fabrics, secondary weathering processes (brecciation and changes in the magnetomineralogy), and compaction. Nevertheless, P′ values generally decrease with proximity to the unconformity (Fig. 7b), and there is a weak, but positive relation between κ_{bulk} and P′, at least below the laterite (see regression curve in Fig. 9b). There is no clear correlation between shape factor T and weathering degree within the saprock–saprolite zone (Fig. 7c).

The AMS ellipsoid axes are variously oriented. The unweathered and macroscopically undeformed granite sample (RA3-1) has shallowly to moderately N or S plunging poles of magnetic foliation (κ_3) and horizontal, W–E trending magnetic lineations (κ_1) (Fig. 10: type 1). The unweathered granite corestone (RA1-5a) shows a girdle distribution of κ_3 around a moderately inclined and NE trending κ_1 (Fig. 10: type 1/2). The weathering-breccias of the saprock and saprolite zones have a similar pattern to RA1-5a, and a few of them resemble the axes distribution as seen in RA3-1 (Fig. 10: type 1, type 1/2, type 2). Laterite samples (RA2-1b, RA2-2) have steeply inclined κ_3 and N–S trending, flat-lying κ_1 (Fig. 10: type 3). Microscale image analysis shows that this magnetic fabric resembles the petrographic fabric defined by the SPO of Fe–Mg–micas (Angerer, 2007). One laterite sample (RA2-1a) shows an AMS pattern quite similar to

Table 2
AMS data and fabric types of all samples and AMS cylinders from the Roded weathering profile.

Sample	Distance [m]	Lithology	AMS sample specimen	AMS fabric-type	κ_{bulk} [$\times 10^{-6}$]	P′	T	κ1	κ2	κ3
RA3-1	~50	Granite	RA3-1_I	1	1650	1.067	0.557	97/13	300/76	188/5
RA3-1	~50	Granite	RA3-1_II	1	1291	1.059	0.216	87/35	269/55	178/1
RA3-1	~50	Granite	RA3-1_III	1	2092	1.094	0.092	88/23	331/46	195/35
RA3-1	~50	Granite	RA3-1_IV	2	629	1.04	0.016	16/28	272/25	147/52
RA3-1	~50	Granite	RA3-1_V	1	2810	1.067	0.506	285/5	18/33	187/56
RA3-1	~50	Granite	RA3-1_VI	2	608	1.056	−0.893	209/4	116/36	305/53
RA1-1A	14.5	Foliated granite	RA1-1A_I	2	457	1.068	0.153	239/32	351/31	114/43
RA1-1A	14.5	Foliated granite	RA1-1A_II	2	573	1.112	0.034	251/48	357/14	98/38
RA1-1A	14.5	Foliated granite	RA1-1A_III	2	672	1.105	−0.201	251/56	21/24	122/23
RA1-1A	14.5	Foliated granite	RA1-1A_IV	2	225	1.048	0.367	236/41	30/47	135/13
RA1-1A	14.5	Foliated granite	RA1-1A_V	2	501	1.093	0.292	253/40	4/23	116/41
RA1-1B	14.0	Foliated granite	RA1-1B_I	2	898	1.061	0.211	230/8	109/75	322/13
RA1-1B	14.0	Foliated granite	RA1-1B_II	2	1255	1.061	−0.382	235/36	70/53	330/7
RA1-1B	14.0	Foliated granite	RA1-1B_III	2	1099	1.066	0.417	236/34	68/55	330/6
RA1-1B	14.0	Foliated granite	RA1-1B_IV	2	1536	1.103	0.498	241/48	77/41	340/8
RA1-1B	14.0	Foliated granite	RA1-1B_V	2	689	1.059	0.438	236/34	58/56	327/1
RA1-3A	6.5	W-breccia	RA1-3A_I	1/2w	170	1.107	−0.245	345/29	247/15	133/57
RA1-3A	6.5	W-breccia	RA1-3A_II	1/2w	145	1.060	−0.341	340/52	96/19	198/32
RA1-3A	6.5	W-breccia	RA1-3A_III	1	141	1.051	0.690	287/18	26/25	165/59
RA1-3A	6.5	W-breccia	RA1-3A_IV	1/2w	288	1.052	−0.192	178/4	323/85	88/3
RA1-3A	6.5	W-breccia	RA1-3A_V	1/2w	333	1.073	0.264	323/13	57/15	195/70
RA1-3A	6.5	W-breccia	RA1-3A_VI	1	193	1.053	−0.282	116/2	25/18	214/72
RA1-3C	6.0	W-breccia	RA1-3C_I	1/2w	619	1.032	0.615	358/21	108/41	248/42
RA1-3C	6.0	W-breccia	RA1-3C_II	1/2w	577	1.030	−0.247	148/12	53/24	263/63
RA1-3C	6.0	W-breccia	RA1-3C_III	1/2w	483	1.027	0.524	5/20	119/50	261/34
RA1-3C	6.0	W-breccia	RA1-3C_IV	1/2w	404	1.015	−0.241	352/0	83/40	262/50
RA1-3C	6.0	W-breccia	RA1-3C_V	1/2w	691	1.036	0.285	359/57	125/21	225/24
RA1-3C	6.0	W-breccia	RA1-3C_VI	1/2w	417	1.033	−0.315	337/54	103/23	205/27
RA1-3B	5.5	W-breccia	RA1-3B_I	1/2w	257	1.044	0.254	36/0	304/80	126/10
RA1-3B	5.5	W-breccia	RA1-3B_III	1/2w	240	1.059	0.145	25/60	228/28	132/10
RA1-3B	5.5	W-breccia	RA1-3B_IV	1/2w	302	1.030	0.516	16/33	234/51	119/19
RA1-3B	5.5	W-breccia	RA1-3B_V	1/2w	320	1.069	−0.289	348/25	206/59	86/16
RA1-3B	5.5	W-breccia	RA1-3B_VI	1/2w	239	1.063	−0.105	41/52	285/19	183/31
RA1-4B	5.0	W-breccia	RA1.4B_III	1/2w	89	1.016	−0.947	30/64	188/24	282/9
RA1-4B	5.0	W-breccia	RA1-4B_I	1/2w	96	1.033	−0.202	43/52	294/14	195/35
RA1-4B	5.0	W-breccia	RA1-4B_II	1/2w	122	1.050	0.072	16/49	113/6	208/41
RA1-4B	5.0	W-breccia	RA1-4B_IV	1/2w	103	1.020	0.034	62/55	234/35	327/4
RA1-4B	5.0	W-breccia	RA1-4B_V	1/2w	100	1.013	0.474	61/56	176/15	274/29
RA1-4B	5.0	W-breccia	RA1-4B_VI	1/2w	183	1.026	0.535	353/51	117/25	222/29
RA1-5A	3.5	Foliated granite	RA1-5A_I	1/2	893	1.079	−0.291	53/57	154/7	249/32
RA1-5A	3.5	Foliated granite	RA1-5A_II	1/2	1260	1.084	−0.662	50/34	170/37	292/35
RA1-5A	3.5	Foliated granite	RA1-5A_III	1/2	1178	1.042	0.048	44/44	135/1	226/46
RA1-5A	3.5	Foliated granite	RA1-5A_IV	1/2	832	1.041	0.408	62/53	318/10	221/35
RA1-5A	3.5	Foliated granite	RA1-5A_V	1/2	1173	1.064	−0.730	76/47	168/2	260/43
RA1-5B	3.5	W-breccia	RA1-5B_I	1/2w	170	1.056	−0.053	37/24	248/63	133/12
RA1-5B	3.5	W-breccia	RA1-5B_III	1/2w	173	1.065	−0.595	31/56	232/33	136/10
RA1-5B	3.5	W-breccia	RA1-5B_IV	1/2w	196	1.022	0.051	26/47	174/38	277/16
RA1-5B	3.5	W-breccia	RA1-5B_V	1/2w	281	1.084	0.291	55/59	163/10	259/29
RA1-5B	3.5	W-breccia	RA1-5B_VI	1/2w	261	1.055	0.347	2/54	265/5	171/36
RA1-6B	2.0	Saprolite	RA1-6B_I	–	142	1.027	−0.733	34/82	268/5	178/6
RA1-6B	2.0	Saprolite	RA1-6B_II	1/2w	103	1.016	0.140	23/20	289/11	172/67
RA1-6B	2.0	Saprolite	RA1-6B_III	–	134	1.017	−0.833	118/6	222/69	26/20
RA1-6B	2.0	Saprolite	RA1-6B_IV	–	109	1.008	−0.462	77/23	328/37	191/44
RA1-6B	2.0	Saprolite	RA1-6B_V	1/2w	125	1.016	0.149	37/60	305/1	214/30
RA1-6B	2.0	Saprolite	RA1-6B_VI	–	105	1.016	−0.263	102/19	323/66	197/15
RA1-7	1.5	Saprolite	RA1-7_I	1/2w	72	1.053	−0.259	164/76	65/2	334/14
RA1-7	1.5	Saprolite	RA1-7_II	1/2w	83	1.018	−0.374	344/30	247/13	136/57
RA1-7	1.5	Saprolite	RA1-7_III	1/2w	50	1.055	−0.659	3/47	151/39	255/16
RA1-7	1.5	Saprolite	RA1-7_IV	1/2w	53	1.050	−0.524	347/53	156/37	250/5
RA1-7	1.5	Saprolite	RA1-7_V	1/2w	92	1.040	0.351	53/80	295/5	205/9
RA1-7	1.5	Saprolite	RA1-7_VI	1/2w	104	1.018	−0.464	37/73	245/16	152/8
RA2-3	1.0	Foliated Laterite	RA2-3_i	2_lat	417	1.016	0.305	136/3	231/64	44/26
RA2-2	0.5	Foliated Laterite	RA2-2_I	3a	424	1.029	0.487	209/16	305/19	83/65
RA2-2	0.5	Foliated Laterite	RA2-2_II	3a	446	1.024	0.639	8/23	266/26	134/54
RA2-2	0.5	Foliated Laterite	RA2-2_III	3a	416	1.035	0.701	16/2	285/25	111/65
RA2-2	0.5	Foliated Laterite	RA2-2_IV	3a	430	1.030	0.456	9/16	271/26	127/59
RA2-2	0.5	Foliated Laterite	RA2-2_V	3a	451	1.034	0.660	5/12	268/30	114/57
RA2-1A	0.2	Foliated Laterite	RA2-1A_I	2_lat	1145	1.028	0.598	100/7	198/49	5/40
RA2-1A	0.2	Foliated Laterite	RA2-1A_II	2_lat	967	1.021	0.803	293/13	187/50	33/37
RA2-1A	0.2	Foliated Laterite	RA2-1A_III	2_lat	862	1.023	0.743	297/8	197/51	34/38
RA2-1A	0.2	Foliated Laterite	RA2-1A_IV	2_lat	879	1.022	0.561	115/17	240/62	18/22
RA2-1B	0.2	Foliated Laterite	RA2-1B_I	3b	389	1.010	0.035	47/2	138/15	309/75
RA2-1B	0.2	Foliated Laterite	RA2-1B_II	3b	433	1.008	0.237	13/4	283/4	155/84
RA2-1B	0.2	Foliated Laterite	RA2-1B_III	3b	437	1.014	0.153	29/7	119/3	228/83
RA2-1B	0.2	Foliated Laterite	RA2-1B_IV	3b	469	1.008	0.587	359/1	269/4	97/86

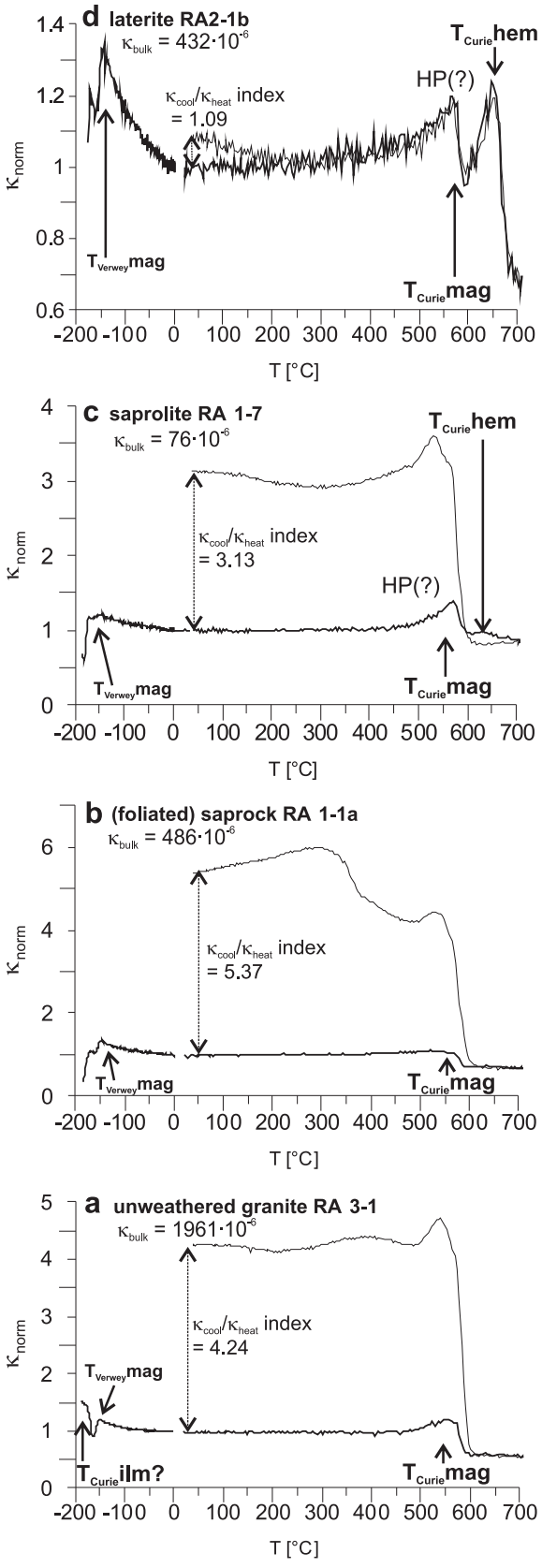

Fig. 8. Temperature-dependent susceptibility, κ(T-ambient after cooling)/κ (T-ambient before heating), of selected samples from the four weathering zones in the profile. Important indicative temperature steps and $\kappa_{cool}/\kappa_{heat}$ indices are indicated.

patterns observed in unweathered and saprolite samples (Fig. 10: type 1). The samples that show clearly S_{2g} deformations (RA1-1a, b) are defined by shallowly inclined κ_3 plunging towards NW or SE. Magnetic lineations plunge shallowly towards SW, indicating an association to the rock fabric.

Magnetic fabrics are heterogeneously distributed at the sample scale. The AMS ellipsoids of each specimen are grouped into four AMS types (Table 2, Fig. 10). Four fabric types can be distinguished, called type 1 (magmatic S_{1m}), type 2 (S_{2g}), type 1/2 (S_{2g} overprinting S_{1m}), and type 3 (S_{3d} crenulation cleavage), respectively. The S_{2g} and S_{3d} fabric domains are relatively well represented by the axes orientation of corresponding AMS fabrics (Fig. 4d, f, g).

7.1. AMS type 1 – first, magmatic/tectonic fabric (S_{1m})

AMS type 1 is developed in samples of all weathering zones (Fig. 10). This AMS pattern has subhorizontal κ_1, which trends in a WNW–ESE direction. κ_3 is NNE–SSW trending with a subhorizontal to medium steep inclination. P′ and κ_{bulk} values are high in the unweathered granite and low in more weathered parts of the profile. This is partly related to the generally positive correlation of P′ and κ_{bulk} below the laterite (Fig. 9b), but also to the overprint by weathering-brecciation. Ellipsoid shapes of type 1 are mostly oblate ($0 < T < 0.8$). Structural overprint at the specimen scale by foliations S_{2g} or S_{3d} leads to changes of the AMS pattern. AMS type 1 exhibits relatively high, mostly positive T values. Therefore, a composite magnetic fabric, which is usually characterized by low T (c.f., Borradaile, 1988; Debacker et al., 2004), is unlikely, taking into account that in all other AMS types within the profile T is lower than in type 1.

AMS type 1 is associated with S_{1m}, the primary granitic fabric in the macroscopically undeformed granite. Martite cluster shapes with poicilitic relic magnetites define a distribution-AMS in the fresher granites. The decrease of ellipsoid definition in those weathered granites showing AMS type 1 (Fig. 10) indicates that the oblate martite shapes still define the bulk AMS, but with a significant reduction of intensity. Here, shape anisotropies of non-interacting magnetite particles, which are randomly oriented relative to the preferred martite orientation, increase their influence and cause weaker anisotropies.

7.2. AMS type 2—second, tectonic foliation (S_{2g})

Type 2 is characteristic for the S_{2g}-foliated granites in the lower part of the profile. κ_3 is subparallel with the NW–SE trending and shallowly inclined S_{2g}-foliation poles. κ_1 plunges moderately towards SW. The magnetic lineation parallels the SW plunging intersection lineation of S_{2g} surfaces (Fig. 10). AMS ellipsoid shapes are mostly oblate ($T < 0.5$) and eccentricity P′ is between 1.05 and 1.09. Type 2 is preserved from the base of the section up to the saprolite horizon.

Type 2 is distinct from type 1 by generally higher eccentricity ($P = 1.04$ to 1.12) and the κ_1 axis directions (Fig. 10). The correlation between κ_1 and the S_{2g} intersection lineation is the result of the superposition of the cleavage-related subfabrics (Borradaile, 1988). As in type 1, interaction of magnetite grains within and between martite grains defines these subfabrics (Angerer, 2007). The SPO of the weakly flattened martites parallels the S_{2g} surfaces. This preferred orientation of martites parallel with S_{2g} surfaces increased the eccentricity P′ of the AMS ellipsoids.

7.3. AMS type 1/2—S_{1m}-fabric overprinted by S_{2g}-fabric

The AMS type 1/2 represents a magnetic fabric that displays characteristics of both the type 1 and 2 fabrics. Type 1/2 is present in unweathered granite inside the corestone (RA1-5a: Fig. 11a) and

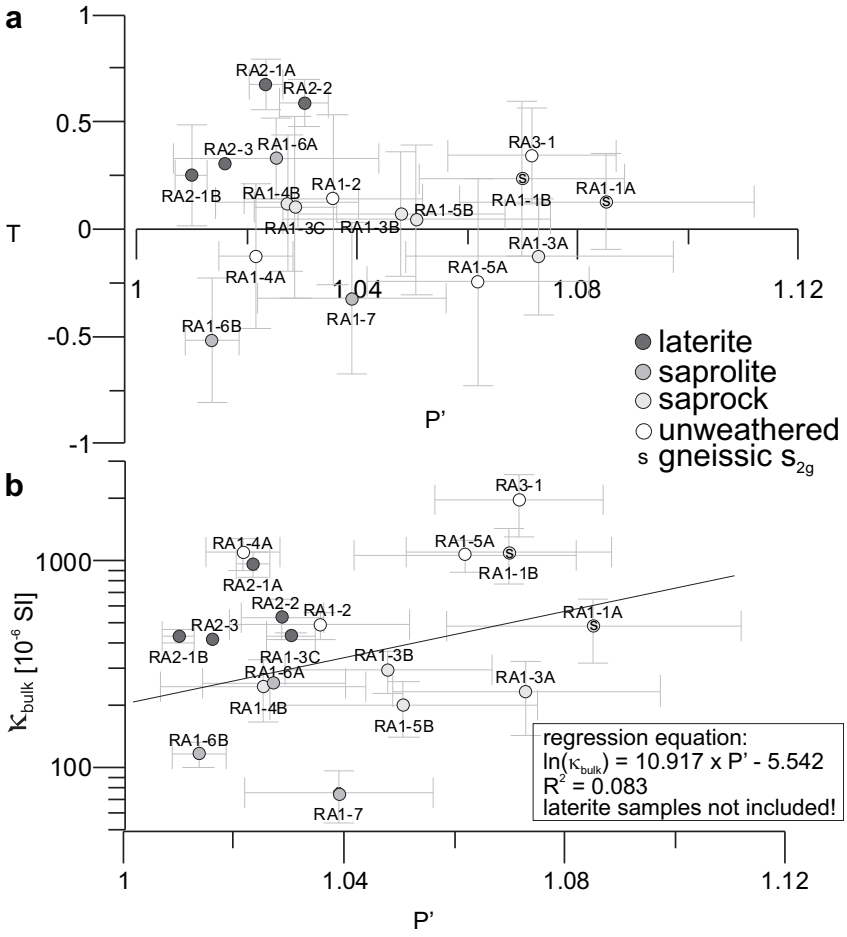

Fig. 9. AMS parameters of samples from the weathering zones: (a) Jelinek diagram, P′ - T; (b) P′ - κ_{bulk} with logarithmic regression curve through all samples except for laterite.

in weathering-breccias throughout the saprock and saprolite zone. κ_1 plunges to the NE in AMS type 1/2. The magnetic foliation poles κ_3, located in the SW and NW quadrants of the stereonet, display a girdle distribution (Fig. 11b) and represent S_{1m} (subvertical E–W) and S_{2g} (subvertical SW–NE). κ_1 correlates geometrically with the lineation of the composite rock fabric. κ_3 shows a great circle distribution around κ_1. The proposed evolution of the superposition of S_{2g} over S_{1m} surfaces is shown in Fig. 5c and d. Superposition is consistent with the ellipsoid parameters of type 1/2 as compared with the parameters of the AMS types 1 and 2 (Fig. 11c,d): P′ values of type 1/2 are small and shapes are spherical to prolate ($T < 0$), whereas both type 1 and type 2, show high P′ values and oblate shapes ($T > 0$).

AMS fabrics of weathering-brecciated rocks are similar to the AMS type 1/2 in the corestone granite. κ_3 scatters along a great circle around the well-clustered NE–NNE trending κ_1-axis. It is inferred that the AMS type 1/2 of the corestone represents the magnetic fabric of most rocks in the saprock–saprolite before weathering-brecciation led to a girdle distribution of κ_3.

7.4. AMS type 3 – laterite cleavage S_{3d}

AMS type 3 occurs exclusively in the laterite (samples RA2-1b and RA2-2). κ_1 is oriented horizontally in NNE direction, and κ_3 lies between the poles of foliation S_{2g} and the unconformity-parallel compaction fabric S_{3d} (Fig. 10). A deformation sequence with changing rock fabrics within the uppermost metre of the lateritic zone is indicated. 0.5 m beneath the unconformity (sample RA2-2), foliation S_{2g} dominates the magnetic foliation, whereas 0.2 m beneath the unconformity (sample RA2-1b), the subhorizontal foliation S_{3d} influences the orientation of κ_3-axes. This AMS fabric is the result of the superposition of S_{1m} and/or S_{2g} fabrics by the compaction crenulation cleavage S_{3d}. Foliation overprint creates a resulting magnetic lineation in the direction of the intersection lineation.

Martitization is advanced in the laterites, thus the abundance of magnetite inclusions in martite grains is reduced. The combination of a weak magnetite anisotropy and high paramagnetic anisotropy characterizes the AMS ellipsoids in type 3. This combination results in low eccentricities (P′ = 1.01 to 1.02) but well defined oblate ellipsoid shapes and distinct axes distribution. As a consequence, fabric type 3, corresponding to S_{3d}, is characterized by a strong planar fabric with SPO of subhorizontal orientation. AMS fabric type 1, with respect to axes orientations, is also observed in a few laterite samples. It is likely that compaction did not change the primary AMS fabric significantly in this case. This interpretation can be explained in light of the greater κ_{bulk} (about 1000×10^{-6} [SI]; Fig. 10) than in the other laterite samples (about 400×10^{-6} [SI]). The larger κ_{bulk} is due to a greater magnetite contents in martite. Martite rearrangement by vertical compaction is negligible and the high inherent AMS intensity of the magnetite-dependent (ferrimagnetic) S_{1m} fabric dominates over the overprinting S_{3d}-related (paramagnetic and antiferromagnetic) AMS. Neither the advanced martitization, nor the martite shape changes due to dissolution exert an important influence on AMS axes distribution in the laterite.

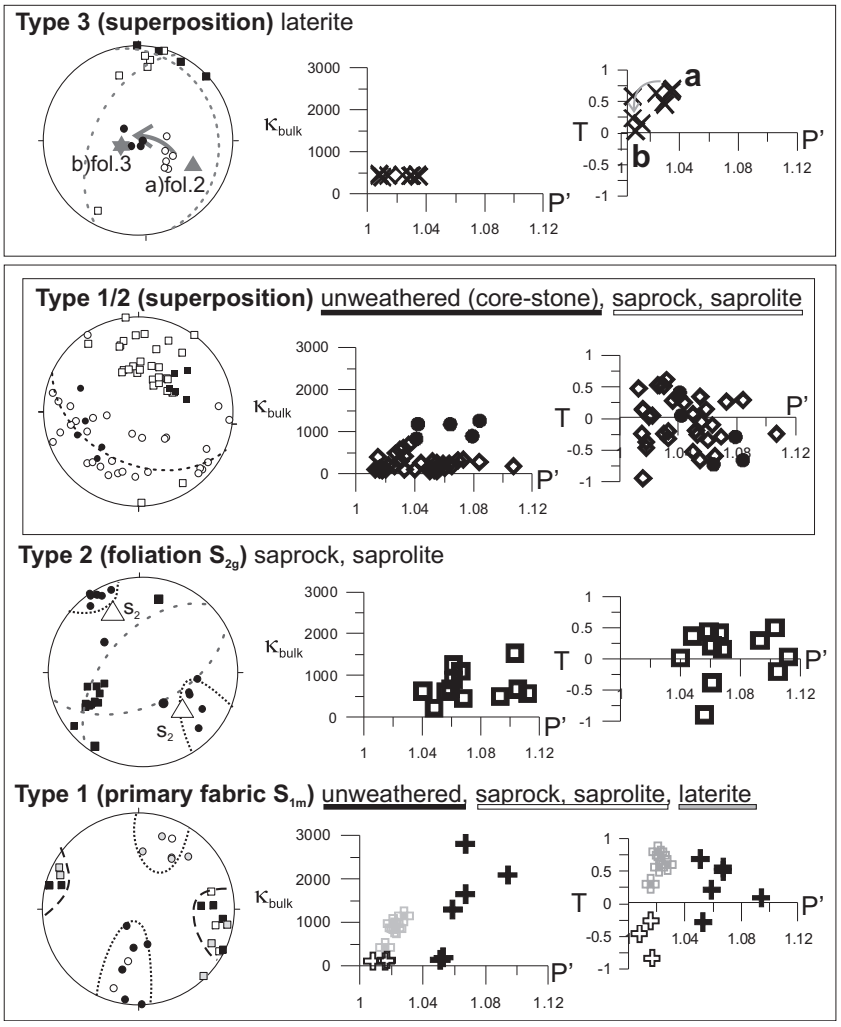

Fig. 10. AMS fabric types. Type 1 (primary granitic fabric) and type 2 (foliated granite) are early fabrics in the granite and persist in all weathering stages. Type 1/2 is a superposition fabric in granite and weathering-breccias. Type 3 occurs in laterite and in the uppermost saprolite (mottled zone). It reveals a progressive imprint of the diagenetic compaction foliation S_{3d}. Black symbols represent granite, saprock and saprolite samples, white symbols represent laterite.

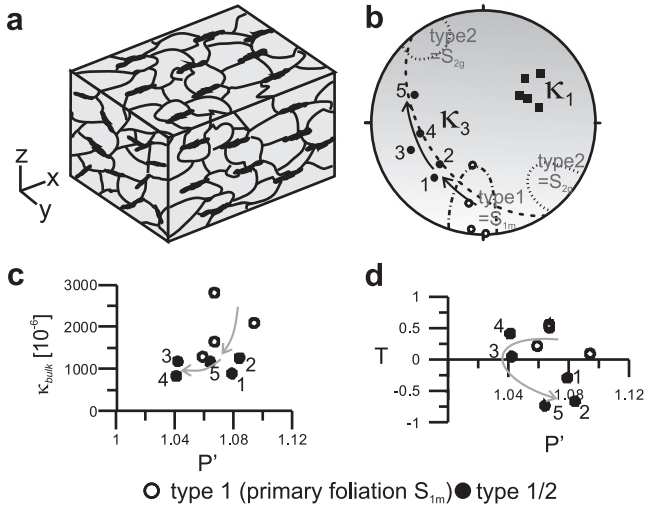

Fig. 11. Rock and AMS fabric type 1/2 developed in fresh granite from a corestone (sample RA1-5a); (a) granite texture dominated by intersection lineations of subfabrics S_{1m} and S_{2g} (lineations highlighted); (b) lower hemisphere projection of AMS axes, showing κ_3 of type 1/2 between κ_3 of types 1 and 2; (c) P′ - κ_{bulk} diagram, and (d) Jelinek diagram, P′ – T, with ellipsoid parameters related to type 1-type 2 overprinting. The arrows follow a path from type 1 to type 1/2.

8. Discussion and conclusions

The present study distinguished four fabric types in the Roded Granite beneath the basement–cover interface (Figs. 2, 11 and 12). Early, Pan-African fabrics (S_{1m}, S_{2g}), are overprinted in a palaeo-weathering zone from bottom to top with a saprock–saprolite–laterite-profile. Weathering prior to early Cambrian sedimentation lead to sub-surface physical weathering-brecciation in saprock and saprolite, and intense chemical weathering with clay-formation in saprolite and laterite. The youngest fabric type (S_{3d}) in the upper laterite is defined by a strong SPO of relic Fe–Mg–mica and clay minerals. It is oriented subhorizontally and subparallel with the basement–cover interface (Figs. 4, 6, 11 and 12), and is related to compaction. In the laterite, an enrichment of haematite and relic Fe–Mg–mica led to increase of κ_{bulk} (Figs. 2, 3, 7 and 10). Weathering degree in saprock and saprolite (mainly brecciation) and in lower, less-compacted laterite (clay precipitation) is an important factor controlling the intensity and shape of AMS ellipsoids, whereas it is less important for changes of axial directions. In much of the laterite, a correspondence between compaction ($C_{section}$) and κ_3-inclination is shown by a negative linear relation between both parameters (Fig. 6g). This shows that AMS ellipsoid orientations are a good

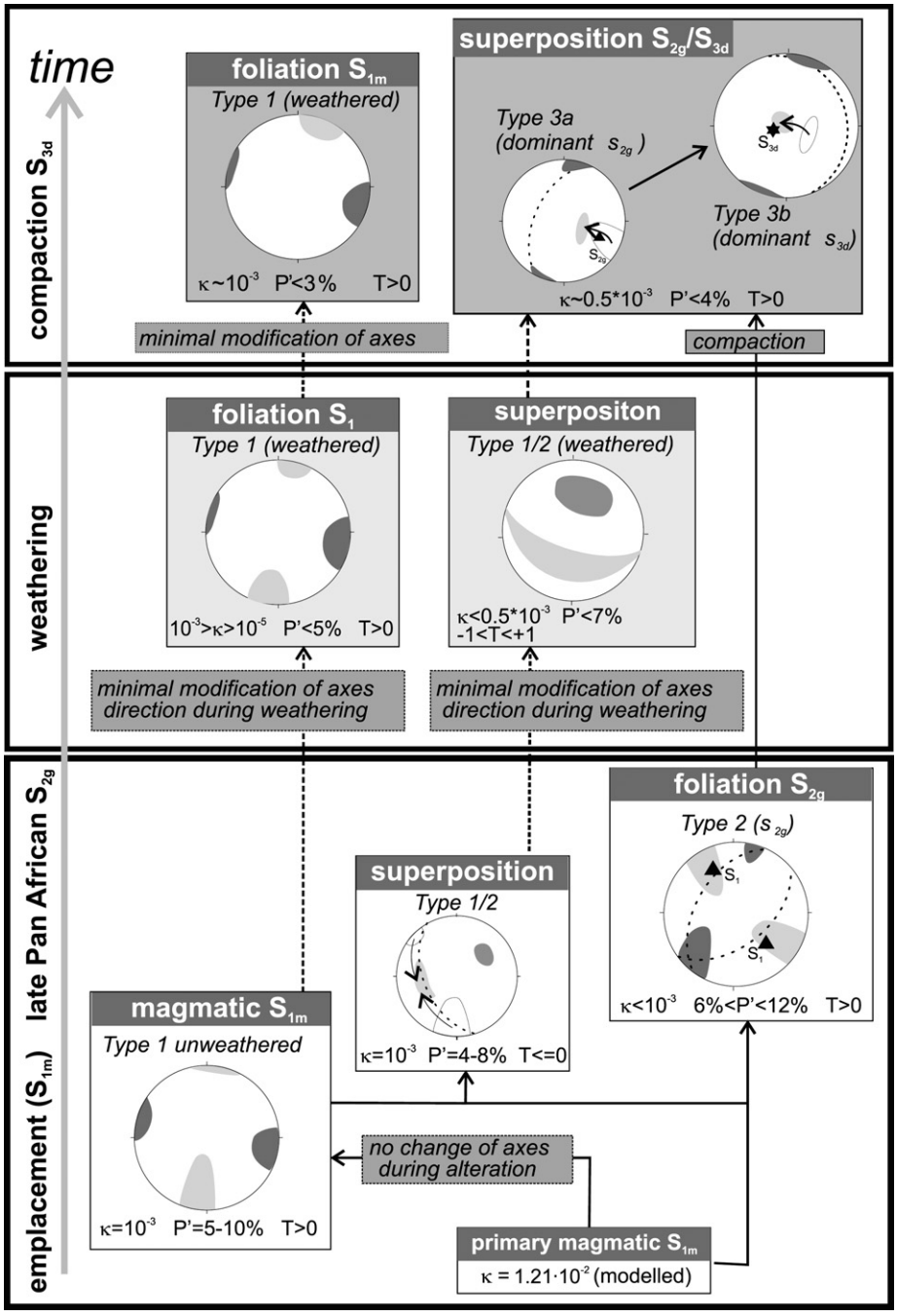

Fig. 12. The evolution of the AMS in the Roded Granite. The magnetic fabric of the primary, unaltered granite is not preserved, but its κ_{bulk} is modelled (Angerer, 2007). See text for details.

marker for the progressive overprint of horizontal compaction (S_{3d}) over primary fabrics (S_{1m} and S_{2g}; Figs. 11 and 12).

Following Byerlee's law (Byerlee, 1978; Scholz, 1990, 2002), the critical shear strength τ at which shear occurs with the effective stress σ_e along a surface is

$$\tau = \mu_F \times \sigma_e \quad (3)$$

The coefficient of sliding friction, μ_F ($0 < \mu_F < 1$), is lithologically controlled and expected to be small along the boundary between laterite (clay-rich rock) and the saprolitic granite (lower boundary of laterite), and between laterite and redbeds (upper boundary). Analogous to the reactivation-susceptibility of phyllosilicate-rich fault zones (e.g., Wintsch et al., 1995 and references therein), the clay enrichment and the compaction-induced SPO parallel with the basement–cover interface provide a plausible explanation for the susceptibility of decollement nucleation and -development at and/or beneath basement-cover interfaces.

Additional factors of similar importance may be permeability and hydraulic conductivity in the weathering zones. In the saprolite and saprock, the permeability is high due to intensely jointed weathering-breccias. In contrast, vertical permeability is low in the laterite, due to the anisotropy caused by the compaction and sub-horizontal S_{3d}. The sealing character of such a highly anisotropic SPO of phyllosilicates is well known (Kopf, 2001; Zhu and Wong,

1997). A joint system, which could increase the vertical hydraulic conductivity, is not present in the laterite. As a consequence, the impermeable phyllosilicate-rich laterite horizon just beneath the basement–cover interface is a hydraulic barrier. Such impermeable layers in the crust can cause considerable decrease in the critical shear strength τ, if fluid pressure increases due to fluid trapping by the impermeability (e.g., Axen, 1992; Handin et al., 1963; Scholz, 2002) and, ultimately, facilitate the formation of a decollement shear zone at the top of the basement rocks (e.g., Gupta and Bickle, 2004; Kopf, 2001). A potential cause for the fluid pressure increase could be tectonic loading, for example due to the development of an accretionary or orogenic wedge (e.g., Calderoni et al., 2009; Mourgues and Cobbold, 2006).

In conclusion, the present study shows the development of potentially weak horizons in crystalline rocks beneath the basement surface or basement–cover interface, genetically related to lateritic paleaoweathering. The mechanical weakness of a clay-enriched weathering horizon with a subhorizontal and planar SPO combined with the potential for creating an overpressured state due to the sealing character of such a zone provides a viable explanation for the abundant localization of decollement horizons at or beneath basement–cover interfaces.

Acknowledgements

This study is part of the first authors' doctoral thesis, which was undertaken at Geologisch–Paläontologisches Institut, Universität Heidelberg within the Graduiertenkolleg 273 "Fluid-rock interaction". The authors thank Deutsche Forschungsgemeinschaft for financing the doctoral studies, and Karlsruhe Institute of Technology (KIT) for supporting the work on the paper. Many thanks to Agnes Kontny, the head of the magnetic laboratory at Heidelberg University, now at KIT, and Helga de Wall, Erlangen University, for their help in measuring and interpreting the data. We acknowledge the in-depth reviews of Graham Borradaile and Frantisek Hrouda and JSG editor Bill Dunne.

References

Anand, R., Paine, M., 2002. Regolith geology of the Yilgarn Craton, western Australia: implications for exploration. Australian Journal of Earth Sciences 49, 3–162.
Angerer, T., 2007. Fossil palaeoweathering profiles and their relation to deformation at basement-cover-interfaces. Case studies from Israel, Sweden and Spain. PhD Thesis, Ruprecht-Karls-University Heidelberg.
Avigad, D., Sandler, A., Kolodner, K., Stern, R.J., McWilliams, M., Miller, N., Beyth, M., 2005. Mass-production of Cambro-Ordovician quartz-rich sandstone as a consequence of chemical weathering of Pan-African terranes: environmental implications. Earth and Planetary Science Letters 240, 818–826.
Axen, G.J., 1992. Pore pressure, stress increase, and fault weakening in low-angle normal faulting. Journal of Geophysical Research 97, 8979–8991.
Ben-Avraham, Z., Lazar, M., 2006. The structure and development of the Dead Sea basin; recent studies. In: Enzel, Y., Agnon, A., Stein, M. (Eds.): new Frontiers in Dead Sea Paleoenvironmental Research. Special Paper—Geological Society of America 401, 1–13.
Bentor, Y.K., 1985. The crustal evolution of the Arabo-Nubian Massif with special reference to the Sinai Peninsula. Precambrian Research 28, 1–74.
Boivin, P., Schäffer, B., Temgoua, E., Gratier, M., Steinman, G., 2005. Assessment of soil compaction using soil shrinkage modelling: experimental data and perspectives. Soil and Tillage Research 88, 65–79.
Borradaile, G.J., 1988. Magnetic susceptibiliy, petrofabrics and strain. Tectonophysics 156, 1–20.
Butler, R. W. H., Holdsworth, R. E., Matthews, S. J., 2006. Styles of basement involvement in the Moine thrust belt, NW Scotland. Special Paper Geological Society of America 414, 133–151.
Byerlee, J., 1978. Friction of rocks. In: Byerlee, J.D., Wyss, M. (Eds.), Rock friction and earthquake prediction. Pure and Applied Geophysics 116, pp. 615–626.
Calderoni, G., Di Giovambattista, R., Burrato, P., Ventura, G., 2009. A seismic sequence from Northern Apennines (Italy) provides new insight on the role of fluids in the active tectonics of accretionary wedges. Earth and Planetary Science Letters 281, 99–109.
Caudill, M.R., Driese, S.G., Mora, C.I., 1997. Physical compaction of vertic Palaeosols; implications for burial diagenesis and palaeo-precipitation estimates. Sedimentology 44, 673–685.
Coward, M., 1994. Continental Collision. Pergamon Press, Tarrytown, NY. 264–288.
Daly, L., Henry, B., 1983. Separation d'anisotropies magnetiques composantes en vue d'applications a l'etude quantitative de la deformation des roches. Comptes-Rendus des Seances de l'Academie des Sciences, Serie 2: Mecanique-Physique, Chimie, Sciences de l'Univers, Sciences de la Terre 296, 153–156.
Druckman, Y., Weissbrod, T., Garfunkel, Z., 1993. Geological Map of Israel 1:100.000 sheet 25–26 Yotvata and Elat. Geological Survey of Israel, Jerusalem.
Debacker, T.N., Robion, P., Sintubin, M., 2004. The anisotropy of magnetic susceptibility (AMS) in low-grade, cleaved pelitic rocks; influence of cleavage/bedding angle and type and relative orientation of magnetic carriers. In: Martín-Hernàndez, F., Lueneburg, M., Aubourg, C., Jackson, M. (Eds.), Magnetic Fabric; Methods and Applications. Geological Society of London, Special Publications, vol. 238, pp. 77–107.
Garfunkel, Z., 1980. Contribution to the geology of the Precambrian of the Elat area. Israel Journal of Earth-Sciences 29, 25–40.
Garfunkel, Z., 1993. The geological history of Israel; an overview. In: Gavrieli, I. (Ed.): Annual Meeting—Israel Geological Society, Jerusalem, 40.
Garfunkel, Z., 1999. History and paleogeography during the Pan-African orogen to stable platform transition; reappraisal of the evidence from Elat area and the northern Arabian-Nubian Shield. Israel Journal of Earth-Sciences 48, 135–157.
Garfunkel, Z., 2002. Early Paleozoic sediments of NE Africa and Arabia; products of continental-scale erosion, sediment transport, and deposition. Israel Journal of Earth-Sciences 51, 135–156.
Gee, D.G., Fossen, H., Henriksen, N., Higgins, A.K., 2008. From the early Paleozoic platforms of Baltica and Laurentia to the Caledonide orogen of Scandinavia and Greenland. Episodes 31, 44–51.
Gupta, S., Bickle, M.J., 2004. Ductile shearing, hydrous fluid channelling and high-pressure metamorphism along the basement-cover contact on Sikinos, Cyclades, Greece. Geological Society Special Publications 224, 161–175.
Gutkin, V., Eyal, Y., 1998. Geology and evolution of Precambrian rocks, Mt. Shelomo, Elat area. Israel Journal of Earth-Sciences 47, 1–17.
Handin, J., Hager Jr., R.V., Friedman, M., Feather, J.N., 1963. Experimental deformation of sedimentary rocks under confining pressure; pore pressure tests. Bulletin of the American Association of Petroleum Geologists 47, 717–755.
Hrouda, F., 1994. A technique for the measurement of thermal changes of magnetic susceptibility of weakly magnetic rocks by the CS-2 apparatus and KLY-2 Kappabridge. Geophysical Journal International 118, 604–612.
Jarrar, G.H., Wachendorf, H., Zachmann, D., 1993. A Pan-African alkaline pluton intruding the Saramuj Conglomerate, South–west Jordan. Geologische Rundschau 82, 121–135.
Jelinek, V., 1981. Characterization of the magnetic fabric of rocks. Tectonophysics 79, T63–T67.
Just, J., 2005. Modification of magnetic properties in granite during hydrothermal alteration (EPS-1 borehole, Upper Rhine Graben). PhD thesis, Ruprecht-Karls-Universität.
Just, J., Kontny, A., de Wall, H., Hirt, A.M., Martin, H.F., 2004. Development of magnetic fabrics during hydrothermal alteration in the Soultz-sous-Forets granite from the EPS-1 borehole, Upper Rhine Graben. In: Martín-Hernández, F., Lueneburg, M., Aubourg, C., Jackson, M. (Eds.), Magnetic Fabric; Methods and Applications. Geological Society of London, Special Publications, vol. 238, pp. 509–526.
Katz, O., Avigad, D., Matthews, A., Heimann, A., 1998. Precambrian metamorphic evolution of the Arabian-Nubian shield in the Roded area, southern Israel. Israel Journal of Earth-Sciences 47, 93–110.
Kontny, A., de Wall, H., 2000. The use of low and high k(T)-curves for the characterization of magneto-minerological changes during metamorphism. Physics and Chemistry of the Earth 25, 421–429.
Kontny, A., Woodland, A.B., Koch, M., 2004. Temperature-dependent magnetic susceptibility behaviour of spinelloid and spinel solid solutions in the systems $Fe2SiO_4$–Fe_3O_4 and (Fe, Mg)$2SiO_4$–Fe_3O_4. Physics and Chemistry of Minerals 31, 28–40.
Kopf, A., 2001. Permeability variation across an active low-angle detachment fault, western Woodlark Basin (ODP Leg 180), and its implication for fault activation. In: Holdsworth, R.E., Strachan, R.A., Magloughlin, J.F., Knipe, R.J. (Eds.), The Nature and Tectonic Significance of Fault Zone Weakening. Geololgical Society Special Publication, vol. 186, pp. 23–41.
Law, R.D., Butler, R.W.H., Holdsworth, R.E., Krabbendam, M., Strachan, R.A., 2010. Continental Tectonics and Mountain Building; the Legacy of Peach and Horne.
Lister, G.S., Davis, G.A., 1989. The origin of metamorphic core complexes and detachment faults formed during Tertiary continental extension in the northern Colorado River region, U.S.A. Journal of Structural Geology 11, 65–94.
Madritsch, H., Schmid, S.M., Fabbri, O., 2008. Interactions between thin- and thick-skinned tectonics at the northwestern front of the Jura fold and thrust belt (eastern France). Tectonics 27, TC5005. doi:10.1029/2008TC002282.
Mathe, P.E., Rochette, P., Collin, F., Richter, A.K., 1997. The origin of magnetic susceptibility and its anisotropy in some weathered profiles. Physics and Chemistry of the Earth 22, 183–187.
Migon, P., Lidmar, B.K., 2001. Weathering mantles and their significance for geomorphological evolution of Central and Northern Europe since the Mesozoic. Earth-Science Reviews 56, 285–324.
Mourgues, R., Cobbold, P.R., 2006. Thrust wedges and fluid overpressures; sandbox models involving pore fluids. Journal of Geophysical Research 111, 14.
Nemcok, M., Schamel, S., Gayer, R.A., 2005. Thrustbelts: Structural Architecture, Thermal Regimes and Petroleum Systems. Cambridge University Press, Cambridge, United Kingdom.

Nesbitt, H.W., Young, G.M., 1989. Formation and diagenesis of weathering profiles. Journal of Geology 97, 129–147.
Retallack, G.J., 1991. Untangling the effects of burial alteration and ancient soil formation. Annual Review of Earth and Planetary Sciences 19, 183–206.
Roberts, A., Yielding, G., 1994. Continental extensional tectonics. In: Hancock, P.L. (Ed.), Continental Deformation. Pergamon, Oxford, pp. 223–250.
Sobolev, S.V., Petrunin, A., Garfunkel, Z., Babeyko, A.Y., Desert Group, 2005. Thermo–mechanical model of the Dead Sea Transform. Earth and Planetary Science Letters 238, 78–95.
Scholz, C., 1990. The Mechanics of Earthquakes and Faulting. Cambridge University Press, Cambridge.
Scholz, C., 2002. The Mechanics of Earthquakes and Faulting. Cambridge University Press, Cambridge.
Stephens, C.G., 1946. Pedogenesis following the dissection of lateritic regions in southern Australia. Bulletin of the Council for Scientific and Industrial Research—Australia, Commonwealth 206, 1–21.
Stern, R.J., 2002. Crustal evolution in the East African Orogen; a neodymium isotopic perspective. Journal of African Earth Sciences 34, 109–117.
Streule, M.J., Strachan, R.A., Searle, M.P., Law, R.D., 2010. Comparing Tibet–Himalayan and Caledonian crustal architecture, evolution and mountain building processes. Geological Society Special Publications 335, 207–232.
Tardy, Y., 1992. Diversity and terminology of Lateritic profiles. In: Martini, P., Chesworth, W. (Eds.), Weathering, Soils & Paleosols. Developments in Earth Surface Processes, vol. 2. Elsevier, Amsterdam/Oxford/New York/Tokyo, pp. 379–405.
Tarling, D.H., Hrouda, F., 1993. The Magnetic Anisotropy of Rocks. Chapman & Hall, London.
Tauxe, L., 2002. Paleomagnetic Principles and Practice. Kluwer Academic Publishers, Dordrecht.
Weissbrod, T., 1980. The Paleozoic of Israel and adjacent countries (a lithostratigraphic study). PhD thesis, Hebrew Unversity Jerusalem.
Wintsch, R.P., Christofferson, R., Kronenberg, A.K., 1995. Fluid–rock reaction weakening of fault zones. Journal of Geophysical Research 100, 13021–13032.
Zhu, W., Wong, T.F., 1997. The transition from brittle faulting to cataclastic flow; permeability evolution. Journal of Geophysical Research-B: Solid Earth and Planets 102, 3027–3041.